Applied Journal of Physical Science
Volume 7(1), pages 19-33, February 2026
Article Number: 23E551162
ISSN: 2756-6684
https://doi.org/10.31248/AJPS2026.137
https://integrityresjournals.org/journal/AJPS
Full Length Research

Analysis of heat transfer models of electromagnetohydrodynamic potassium dichromate ($K_2Cr_2O_7$) nanofluid flow past through the cylindrical coordinate

Ojo, Adetoye Solomon[1]*, Egbo, Chijioke Aloysius[2] and Nwabuzor, Peter Onyelukachukwu[3]

[1]Department of Physics, University of Port Harcourt, PMB 5323 Choba, Nigeria.
[2]Department of Science Laboratory Technology, Federal Polytechnic of Oil and Gas Bonny, Rivers State.
[3]Department of Physics with Electronics, University of Port Harcourt, PMB 5323 Choba, Nigeria.

*Corresponding author. Email: solomontoye10@gmail.com; Co-authors: chijioke.egbo@gmail.com, peter.nwabuzor@uniport.edu.com

Received 24th January 2026; Accepted 18th February 2026

ABSTRACT: This study presents a theoretical analysis of electromagnetohydrodynamic (EMHD) heat transfer in potassium dichromate ($K_2Cr_2O_7$) nanofluid flow formulated in cylindrical coordinates. The model accounts for the combined influence of electric and magnetic fields, nanoparticle volume fraction, thermal radiation, and viscous dissipation effects on the momentum and thermal boundary layers. The governing nonlinear partial differential equations describing the flow and temperature fields are transformed into a coupled system of nonlinear ordinary differential equations through suitable similarity transformations. To obtain accurate approximate analytical solutions, the Homotopy Perturbation Method (HPM) is employed, providing rapidly convergent series expressions for the velocity and temperature distributions. The effects of key dimensionless parameters, including the magnetic interaction parameter, electric field parameter, Prandtl number, radiation parameter, and nanoparticle concentration, are investigated in detail. The results indicate that an increase in the magnetic parameter significantly reduces the velocity profile due to Lorentz force resistance, whereas a stronger electric field intensity enhances the acceleration of the flow. Furthermore, increasing the nanoparticle volume fraction improves the effective thermal conductivity, leading to a noticeable enhancement in the surface heat transfer rate and Nusselt number. Thermal radiation is found to elevate the temperature distribution and increase the thickness of the thermal boundary layer. Overall, the EMHD mechanism provides an efficient means of controlling heat transfer in cylindrical nanofluid transport systems. The outcomes of this work are relevant to the design of advanced electromagnetic thermal management devices, energy conversion systems, and nanofluid-based cooling technologies.

Keywords: Cylindrical coordinates, electromagnetohydrodynamic, heat transfer models, Homotopy Perturbation Method, potassium dichromate.

INTRODUCTION

Electromagnetohydrodynamic (EMHD) and magnetohydrodynamic (MHD) nanofluid flows continue to attract extensive research attention due to their critical roles in enhancing heat transfer performance across a wide range of engineering applications, including thermal management systems, energy conversion devices, electronic cooling, and industrial heat exchangers. Nanofluids—engineered suspensions of nanoscale particles in base fluids—offer superior thermal transport properties compared with conventional fluids, owing to enhanced thermal conductivity and convective heat transfer characteristics. When these nanofluids interact with externally applied electric and magnetic fields, complex momentum and energy transport phenomena arise that can be utilised to control flow behaviour and optimise thermal performance (Ali *et al.,* 2020; Nikodijević Đorđević *et al*., 2025).

Research into entropy generation and second-law thermodynamic optimisation in EMHD/MHD nanofluid systems has emphasised the balance between heat transfer enhancement and irreversibility reduction. For instance, investigations of MHD nanofluid flows in porous

media demonstrate how entropy production is influenced by magnetic forcing, viscous dissipation, and thermal gradients, revealing key insights into system inefficiencies and thermal optimisation strategies (Albqmi and Sivanandam, 2024; Zahor *et al.,* 2024).

Advances in modelling techniques have significantly enriched the literature. Analytical approaches incorporating heat flux models such as Cattaneo–Christov have illustrated the importance of non-Fourier effects in heat transfer, particularly when coupled with EMHD and Darcy–Forchheimer flow mechanisms (Jameel *et al*., 2024; Pheko *et al*., 2025). Studies employing machine learning and data-driven frameworks have further expanded predictive capabilities, enabling accurate simulation of complex dual diffusive flows and stratified Maxwell fluids under combined electromagnetic influences (Aljaloud *et al*., 2025).

A growing body of literature has focused on optimisation and sensitivity analysis of EMHD flows under various physical conditions. Znaidia *et al*. (2025) conducted a sensitivity investigation of radiative nanofluid flow over a melting surface, quantifying the effects of thermal conductivity and effective viscosity on heat transfer performance in the presence of magnetic fields. Similarly, hybrid nanofluid studies have explored interactions between different nanoparticle combinations and EMHD effects, revealing enhanced transport phenomena when compared to conventional nanofluid systems (Nikodijević Đorđević *et al*., 2025).

In parallel, entropy distribution analyses for generalised fluids subjected to classical versus non-Fourier heat conduction laws have deepened understanding of how thermodynamic irreversibility evolves under varying transport assumptions. These investigations demonstrate that non-classical heat flux models can significantly modify entropy profiles and system efficiencies in inclined channel flows and related configurations.

Recent research has also incorporated machine learning-driven prediction models, including ANN-based frameworks for MHD radiative heat transfer and Darcy–Forchheimer squeezing flows of hybrid nanofluids with chemical reactions. These methods not only provide accurate temperature and velocity predictions but also optimise thermal performance in complex flow scenarios, including autocatalytic and multi-parameter interactions.

Despite these considerable advances, most studies focus on Cartesian or simplified geometries, leaving the EMHD nanofluid behaviour in cylindrical coordinate systems underexplored. Cylindrical configurations are highly relevant in pipes, tubes, rotating machinery, and reactor designs where curvature and radial gradients exert a pronounced influence on heat transfer and fluid motion. For example, turbulence, boundary layer development, and radial heat diffusion are all affected by geometry, magnetic field intensity, nanoparticle concentration, and radiative effects in ways that differ fundamentally from planar flow systems (Yasir *et al*., 2025).

Furthermore, many existing studies integrate multiple complicating factors—such as porous media resistance, thermal radiation, slip conditions, and hybrid nanofluid compositions—highlighting the need for comprehensive models that capture the full suite of physical influences. Incorporating advanced heat flux theories, flow resistance mechanisms, and data-driven predictive frameworks into cylindrical EMHD models promises to improve both theoretical understanding and practical design of thermal systems.

Adetoye *et al*. (2025) determined the comparative effects of energy transfer on silver nanofluid in (MHD) flow via the cylindrical surface. They displayed the variation of the material parameters, an increase in Prandtl profile also improves Nusselt profile, as well as an increase in chemical reaction declines Sherwood number of the nanofluid.

The application of the homotopy perturbation (HPM) method in physical sciences and engineering has been the subject of numerous research projects in recent years. Scientists can gain a deeper understanding of fundamental physical processes, optimise technological applications, and resolve urgent physical challenges by analysing the complexities of the homotopy perturbation method. Numerous pioneering scientists have established the foundation for the development of HPM in various fields. The homotopy perturbation method (HPM), proposed by Chinese mathematician He in 1998, is an analytical technique for differential equations at first which also displayed the computer methods in applied mechanics and engineering (He, 1999). Also, the application of homotopy perturbation method in Newtonian fluids was examined and demonstrates that HPM is a robust analytical tool for probing the parameter space of complex heat and mass transfer flows, providing fast and physically intuitive results that can guide more costly numerical simulations and displayed that decrease in Prandtl number in thicker thermal boundary layers, potentially reduces skin friction while High Prandtl number results to thinner thermal boundary layers, potentially increases skin friction (Adetoye *et al*., 2026).

Given this research landscape, the present study examines the heat transfer models of electromagnetohydrodynamic potassium dichromate $(K_2Cr_2O_7)$ nanofluid flow past through cylindrical coordinates, integrating electromagnetic forcing, viscous dissipation, thermal radiation, and nanoparticle effects. By situating this work within the broader context of recent computational, analytical, and machine learning-based investigations, the analysis aims to provide comprehensive insights into EMHD nanofluid transport phenomena in practical cylindrical geometries.

PHYSICAL MODEL AND PROBLEM DESCRIPTION

The physical configuration of the present study is

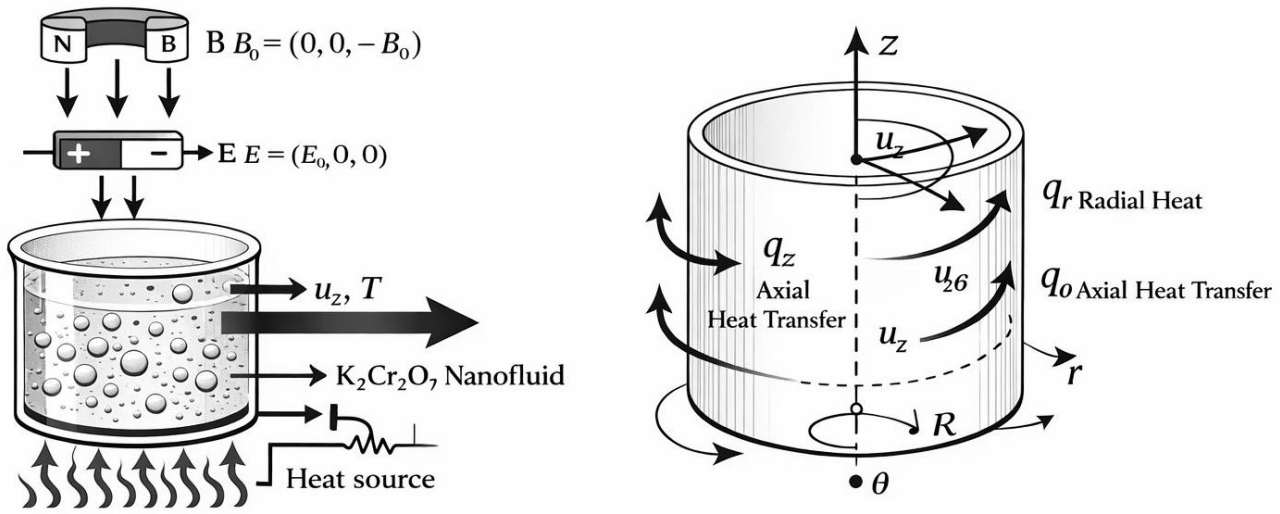

Figure 1. Schematic representation of electromagnetohydrodynamic potassium dichromate $(K_2Cr_2O_7)$ nanofluid flow and heat transfer in cylindrical coordinates.

illustrated in Figure 1. In this work, an electromagnetohydrodynamic (EMHD) flow of potassium dichromate $(K_2Cr_2O_7)$ -based nanofluid is considered in a cylindrical coordinate system (r, θ, z). The analysis focuses on the combined influence of electromagnetic forces and thermal transport mechanisms on the fluid motion and heat transfer characteristics. A uniform external magnetic field of strength B_0 is applied along the axial direction, while an electric field E_0 is imposed perpendicular to the flow direction. These applied fields generate Lorentz forces, which significantly affect the velocity distribution, boundary layer development, and thermal behaviour of the nanofluid. The fluid is assumed to flow primarily in the axial direction z, with the corresponding velocity component denoted by u_z, while the radial coordinate r measures the distance from the cylindrical surface. The cylindrical surface is subjected to a thermal heat source, leading to heat transfer within the nanofluid domain. Both axial and radial heat fluxes are taken into account, represented by q_z and q, respectively. The presence of nanoparticles enhances the effective thermal conductivity of the base fluid, thereby improving the overall heat transfer performance.

The governing equations of mass, momentum, and energy are formulated in cylindrical coordinates by incorporating the effects of electromagnetic body forces, viscous dissipation, and nanofluid thermal properties. The resulting mathematical model provides a framework for investigating the velocity and temperature profiles under various physical parameters.

MATHEMATICAL FORMULATION OF THE PROBLEM

The governing equations describing the flow situation in a cylindrical co-ordinate system with the parameter under investigation can be expressed as the continuity equation, equation of motion, energy equation and concentration equation.

$$\frac{\partial}{\partial x}u_x + \frac{\partial}{\partial t}\rho_{nf} = 0 \tag{1}$$

$$\rho_{nf}\frac{\partial u_x}{\partial t} = -\nabla\rho + \mu_{nf}\nabla^2 u + g\beta_\theta\left(\theta - \theta_*\right) + g\beta_\phi\left(\phi - \phi_*\right) - \sigma B_0^2 u_x - \sigma_0 \tag{2}$$

$$\left(\rho C_p\right)_{nf}\frac{\partial}{\partial x}\theta + \frac{\partial}{\partial x}\left(q_x\right) = K\frac{\partial^2\theta}{\partial x^2} \tag{3}$$

$$\left(\rho C_p\right)_{nf}\frac{\partial}{\partial x}\phi + K_0^2\phi = D\frac{\partial^2\phi}{\partial x^2} \tag{4}$$

In situation where the water base potassium dichromate nanofluid is considered incompressible, and is subjected to a steady state flow condition in the cylindrical coordinate, then equation (2) – (4) with the use of equation (1), transformed into:

$$\frac{\mu_{nf}}{\rho_{nf}}\nabla^2 u - \frac{1}{\rho_{nf}}\nabla\rho + \frac{g\beta_\theta(\theta-\theta_*)}{\rho_{nf}} + \frac{g\beta_\phi(\phi-\phi_*)}{\rho_{nf}} - \frac{\sigma B_0^2 u_x}{\rho_{nf}} - \frac{\sigma_0}{u_x} = 0 \tag{5}$$

$$\frac{1}{(\rho C_p)_{nf}} K\frac{\partial^2}{\partial x^2}\theta - \frac{1}{(\rho C_p)_{nf}}\frac{\partial}{\partial x}(q_x) = 0 \tag{6}$$

$$\frac{1}{(\rho C_p)_{nf}} D\frac{\partial^2}{\partial x^2}\phi - \frac{1}{(\rho C_p)_{nf}} K_0^2\phi = 0 \tag{7}$$

Where T is temperature, v is fluid velocity, ρ is fluid density, P is fluid pressure, μ is the viscosity of fluid, q_x is a radiation term, C_p is specific heat at constant pressure, K_0 is a chemical reaction term, Kr is the thermal conductivity of fluid, C is fluid concentration, and D is chemical molecular diffusivity.

Considering the combination of the mathematical models for effective viscosity models of nanofluid proposed by Brinkman 91947) and Batchelor (1977) models, shown below.

$$\mu_{nf} = \left(\frac{1}{(1-\phi)^{2.5}}\right)\mu_{bf} + \left(1 + 2.5\phi + 6.5\phi^2 + ..\right)\mu_{bf} \tag{8}$$

Also, effective thermal conductivity models used can be expressed as the combination of Xue (2007) and Jang and Choi (2007) models, which is given as:

$$K_{eff} = K_{bf}\frac{1-\phi+2\phi\dfrac{K_{np}}{K_{np}-K_{bf}}In\dfrac{K_{np}+K_{bf}}{2K_{bf}}}{1-\phi+2\phi\dfrac{K_{bf}}{K_{np}-K_{bf}}In\dfrac{K_{np}+K_{bf}}{2K_{bf}}} + K_{bf}(1-\phi) + K_{np}\phi + 3C\frac{d_{bf}}{d_{np}}K_{bf}\,\mathrm{Re}_{d_{np}}^2\,\mathrm{Pr}\,\phi \tag{9}$$

Where ϕ_{np} is the nanoparticle volume fraction, μ_{bf} is the dynamic viscosity of the base fluid, K_B is the Stefan Boltzmann's constant, c is a constant, v is the dynamic viscosity of the base fluid, T is the temperature, r_b is the thickness radius of the base fluid, r_p is the thickness radius of the nanoparticle, d_p is the diameter of the nanoparticle, k_b is the thermal conductivity of the base fluid, k_p is the thermal conductivity of nanoparticle. The radiative heat flux vector q_x of the energy equation (5) is related to the temperature by the expression:

$$\frac{\partial^2 q_x}{\partial y} - 16\sigma\theta_\infty^3\frac{\partial\theta}{\partial x} - 3\sigma^3 = 0 \tag{10}$$

And according to the model proposed by Cogley *et al.* (1968) for an optically thin medium at a relatively low density, the expression for radiative heat flux vector reduces to:

$$\frac{\partial q_x}{\partial y} = 4\alpha^2(\theta-\theta_*) \tag{11}$$

Where $\alpha^2 = \int_0^\infty\left(\delta_k\frac{\partial\omega}{\partial\theta}\right)dk^*$ referred to as the frequency dependent absorption coefficient, and δ_k is the mean absorption

coefficient, σ is the Stefan-Boltzmann constant, ω is the Planck's function, T_o is the temperature at the centre, and T_w is the temperature at the wall. Transforming equation (5) based on the consideration of the radiative flux term, the energy equation becomes.

$$u_x \frac{\partial \theta}{\partial x} = K_{nf} \frac{1}{\left(\rho C_p\right)_{nf}} \left(\frac{\partial}{\partial x} \left(\frac{\partial \theta}{\partial x} \right) \right) - \frac{1}{\left(\rho C_p\right)_{nf}} 4\alpha^2 \left(\theta - \theta_*\right) \tag{12}$$

Hayat *et al* (2021) in their study of convective flow of nanofluid with a wall at ramped temperature, and Tiwari and Das (2007) studied the augmentation of heat transfer of nanofluid on a two-sided lid-driven differential heat cavity. Based on the study of both authors, the density of the nanofluid (ρ_{nf}), thermal expansion due to the temperature of the nanofluid (β_{nf}), thermal expansion due to the concentration of nanofluid (β^*_{nf}), specific heat at constant pressure of nanofluid $\left(C_p\right)_{nf}$ are respectively defined as

$$\phi \frac{\rho_s}{\rho_f} + \left(1 - \phi\right) = \frac{\rho_{nf}}{\rho_f} \tag{13}$$

$$\phi \frac{\beta_s}{\beta_f} + \left(1 - \phi\right) = \frac{\beta_{nf}}{\beta_f} \tag{14}$$

$$\phi \frac{\beta^*_s}{\beta^*_f} + \left(1 - \phi\right) = \frac{\beta^*_{nf}}{\beta^*_f} \tag{15}$$

$$\phi \frac{\left(C_p\right)_s}{\left(C_p\right)_f} + \left(1 - \phi\right) = \frac{\left(C_p\right)_{nf}}{\left(C_p\right)_f} \tag{16}$$

The constant values of some of the thermophysical properties of the materials are presented in Table 1.

DIMENSIONAL ANALYSIS

To tackle the effect of the governing equations, therefore, equations (5) – (7) are transmute into dimensionless form.

$$Sc^{-1} = \frac{D}{\rho C_p}, Gr = Gr_\theta \theta + Gr_\phi \phi, K_0 = \frac{Kr^2 \mu}{\rho C_p}, \mathrm{Re}^{-1} = \frac{\mu}{u_x \rho_{nf}}, \lambda = \frac{\sigma B^2 u_x}{\rho_{nf}}$$

$$\mathrm{Pr}^{-1} = \frac{K}{\rho C_p}, \rho = \frac{1}{\rho} \frac{\partial \rho}{\partial y}, \theta = \frac{\theta - \theta_*}{\theta_*}, R = \frac{16 \varepsilon T_\alpha^3}{3\alpha(\rho C_p)}, \phi = \frac{\phi - \phi_*}{\phi_*}, \sigma_0 = \frac{\sigma_0}{u_x}$$

Where Re implies Reynolds profile, Pr represents Prandtl profile, Sc is Schmidt profile, $Gr_\theta \theta$ is the thermal Grashof number, $Gr_\phi \phi$ is modified Grashof's number, R is dimensionless radiation term, θ is dimensionless temperature, ϕ is dimensionless concentration.

Having employed the dimensionless parameters into equations (5) – (7), transformed into the form

$$\xi_1 \frac{1}{\mathrm{Re}} \frac{\partial^2 u}{\partial y^2} + \xi_2 Gr_\theta \theta + \xi_3 Gr_\phi \phi - \xi_4 \left(\lambda + \sigma_0\right) u = 0 \tag{17}$$

Table 1. Numerical values of thermophysical properties of our materials.

Materials properties	($K_2Cr_2O_7$)	Water (H_2O)
Density ρ (kgm^{-1})	2.676	997.1
Thermal conductivity k (kgm^{-1})	0.54	0.613
Heat capacity C_p $(Wm^{-1}k^{-1})$	750	4179
Thermal expansivity k (kgm^{-1})	3.5×10^{-5}	21×10^{-5}

$$\xi_5 \frac{1}{\Pr} \frac{\partial^2 \theta}{\partial y^2} - \xi_6 R\theta = 0 \tag{18}$$

$$\xi_6 \frac{1}{Sc} \frac{\partial^2 \phi}{\partial y^2} - \xi_6 K_0 \phi = 0 \tag{19}$$

The boundary conditions for equations (7) – (9) imply

$$u = 1, \theta = 1, \phi = 1 \text{ at } x = 0$$

$$u = 0, \theta = 0, \phi = 0 \text{ at } x = 1 \tag{20}$$

From Equation (12) to (15), the ratio of the effective dynamic viscosity terms and the effective thermal conductivity can be expressed as:

$$\xi_1 = \frac{\left(\frac{1}{\left(1-\phi_{np}\right)^{2.5}}\right)\mu_{bf} + \left(1 + 2.5\phi_{np} + 6.5\phi_{np}^2 + ..\right)\mu_{bf}}{\phi\frac{\rho_s}{\rho_f} + \left(1-\phi\right)} \tag{21}$$

$$\xi_2 = \phi\frac{\beta_s}{\beta_f} + \left(1-\phi\right) \tag{22}$$

$$\xi_3 = \phi\frac{\beta_s^*}{\beta_f^*} + \left(1-\phi\right) \tag{23}$$

$$\xi_4 = \frac{1}{\phi\frac{\rho_s}{\rho_f} + \left(1-\phi\right)} \tag{24}$$

$$\xi_5 = \frac{K_{bf}\dfrac{1-\phi+2\phi\dfrac{K_{np}}{K_{np}-K_{bf}}In\dfrac{K_{np}+K_{bf}}{2K_{bf}}}{1-\phi+2\phi\dfrac{K_{bf}}{K_{np}-K_{bf}}In\dfrac{K_{np}+K_{bf}}{2K_{bf}}} + K_{bf}(1-\phi) + K_{np}\phi + 3C\frac{d_{bf}}{d_{np}}K_{bf}\,\mathrm{Re}_{d_{np}}^2\,\Pr\phi}{\phi\dfrac{\left(C_p\right)_s}{\left(C_p\right)_f} + \left(1-\phi\right)} \tag{25}$$

Table 2. Numerical values of coefficients of the hydrodynamic parameters of the dimensionless governing equation when ϕ = 0.02.

Constants	Numerical value
ξ_1	1.136
ξ_2	0.246
ξ_3	0.244
ξ_4	1.012
ξ_5	0.301
ξ_6	0.221

$$\xi_6 = \frac{1}{\phi\dfrac{\left(C_p\right)_s}{\left(C_p\right)_f} + \left(1-\phi\right)} \tag{26}$$

The numerical values of the coefficients of the hydrodynamic parameters of the dimensionless governing equation when ϕ = 0.02 are presented in Table 2.

METHOD OF SOLUTION

Using the Homotopy Perturbation Method to solve equations (17) – (19), given as

$$H(u,p) = (1-p)\left[\xi_1 \frac{1}{\mathrm{Re}} u_{(x)}^{II}\right] + P\left[\xi_1 \frac{1}{\mathrm{Re}} u_{(x)}^{II} + \xi_2 Gr_\theta \theta + \xi_3 Gr_\phi \phi - \xi_4\left(\lambda + \sigma_0\right)u\right] = 0 \tag{27}$$

$$H(\theta,p) = (1-p)\left[\xi_5 \frac{1}{\mathrm{Pr}} \theta_{(x)}^{II}\right] + P\left[\xi_5 \frac{1}{\mathrm{Pr}} \theta_{(x)}^{II} - \xi_6 R\theta\right] = 0 \tag{28}$$

$$H(\phi,p) = (1-p)\left[\xi_6 \frac{1}{Sc} \phi_{(x)}^{II}\right] + P\left[\xi_6 \frac{1}{Sc} \phi_{(x)}^{II} - \xi_6 K_0 \phi\right] = 0 \tag{29}$$

Assume the solution to equations (27) – (29) is written as

$$\begin{aligned} u &= u_0 + pu_1 + p^2 u_2 + \ldots \\ \theta &= \theta_0 + p\theta_1 + p^2\theta_2 + \ldots \\ \phi &= \phi_0 + p\phi_1 + p^2\phi_2 + \ldots \end{aligned} \tag{30}$$

Equation (27) – (29) gives the form, respectively

$$H(u,p) = \xi_1 \mathrm{Re}^{-1} u_{(x)}^{II} + p\xi_2 Gr_\theta \theta_{(x)} + p\xi_3 Gr_\phi \phi_{(x)} - p\xi_4\left(\lambda + \sigma_0\right)u = 0 \tag{31}$$

$$H(u,p) = \xi_5 \mathrm{Pr}^{-1} \theta_{(x)}^{II} - p\xi_6 R\theta = 0 \tag{32}$$

$$H(u,p) = \xi_6 Sc^{-1} \phi_{(x)}^{II} + p\xi_6 K_0 \phi = 0 \tag{33}$$

Substituting equation (30) into equation (31) – (33) the result is

$$\xi_1 \mathrm{Re}^{-1} u_{(x)}^{II} + p\xi_2 Gr_\theta \theta_0 + p^2 \xi_2 Gr_\theta \theta_1 + p^3 \xi_2 Gr_\theta \theta_2 + p\xi_3 Gr_\phi \phi_0 + p^2 \xi_3 Gr_\phi \phi_1 + p^3 \xi_3 Gr_\phi \phi_2 - p\xi_4 (\lambda + \sigma_0) u = 0 \quad (34)$$

$$\xi_5 \mathrm{Pr}^{-1} \theta_{(x)}^{II} - p\xi_6 R\theta_0 - p^2 \xi_6 R\theta_1 - p^3 \xi_6 R\theta_2 = 0 \quad (35)$$

$$\xi_6 Sc^{-1} \phi_{(x)}^{II} + p\xi_6 K_0 \phi_0 + p^2 \xi_6 K_0 \phi_1 + p^3 \xi_6 K_0 \phi_2 = 0 \quad (36)$$

To compare the coefficient of p^0, p^1, p^2, p^3, the result implies

$$p^0: \quad \xi_1 \mathrm{Re}^{-1} u_0^{II} - \xi_4 (\lambda + \sigma_0) = 0 \quad (37)$$

$$p^0: \quad \xi_5 \mathrm{Pr}^{-1} \theta_0^{II} = 0 \quad (38)$$

$$p^0: \quad \xi_6 Sc^{-1} \phi_0^{II} = 0 \quad (39)$$

$$p^1: \quad \xi_1 \mathrm{Re}^{-1} u_1^{II} + \xi_2 Gr_\theta \theta_0 + \xi_3 Gr_\phi \phi_0 = 0 \quad (40)$$

$$p^1: \quad \xi_5 \mathrm{Pr}^{-1} \theta_1^{II} - \xi_6 R\theta_0 = 0 \quad (41)$$

$$p^1: \quad \xi_6 Sc^{-1} \phi_1^{II} + \xi_6 K_0 \phi_0 = 0 \quad (42)$$

$$p^2: \quad \xi_1 \mathrm{Re}^{-1} u_2^{II} + \xi_2 Gr_\theta \theta_1 + \xi_3 Gr_\phi \phi_1 = 0 \quad (43)$$

$$p^2: \quad \xi_5 \mathrm{Pr}^{-1} \theta_1^{II} - \xi_6 R\theta_0 = 0 \quad (44)$$

$$p^2: \quad \xi_6 Sc^{-1} \phi_1^{II} + \xi_6 K_0 \phi_1 = 0 \quad (45)$$

$$p^3: \quad \xi_1 \mathrm{Re}^{-1} u_3^{II} + \xi_2 Gr_\theta \theta_2 + \xi_3 Gr_\phi \phi_2 = 0 \quad (46)$$

$$p^3: \quad \xi_5 \mathrm{Pr}^{-1} \theta_3^{II} - \xi_6 R\theta_2 = 0 \quad (47)$$

$$p^3: \quad \xi_6 Sc^{-1} \phi_3^{II} + \xi_6 K_0 \phi_2 = 0 \quad (48)$$

From equation (20), the modified boundary conditions imply

$$\begin{aligned} &u_0 = u_1 = u_2 = u_3 = 1 \\ &\theta_0 = \theta_1 = \theta_2 = \theta_3 = 1 \\ &\phi_0 = \phi_1 = \phi_2 = \phi_3 = 1 \\ &u_0 = u_1 = u_2 = u_3 = 0 \\ &\theta_0 = \theta_1 = \theta_2 = \theta_3 = 0 \\ &\phi_0 = \phi_1 = \phi_2 = \phi_3 = 0 \end{aligned} \quad (49)$$

Solving equations (37) – (39) by applying the suitable boundary conditions from the equation. The boundary conditions from equation (49) yield the results.

$$u_0 = -\frac{1}{2}\frac{\xi_4 \operatorname{Re}(\lambda+\sigma_0)}{\xi_1}x^2 + \frac{1}{2}\left(\frac{\xi_4 \operatorname{Re}(\lambda+\sigma_0)}{\xi_1} - 2\right)x + 1 \tag{50}$$

$$\theta_0 = -x + 1 \tag{51}$$

$$\phi_0 = -x + 1 \tag{52}$$

Solving equations (40) – (42) by applying the suitable boundary conditions from equation (49), it gives.

$$u_1 = -\frac{1}{2}\frac{\operatorname{Re}\xi_2 Gr_\theta \theta_0}{\xi_1}x^2 - \frac{1}{2}\frac{\operatorname{Re}\xi_3 Gr_\phi \phi_0}{\xi_1}x^2 + \frac{1}{2}\left(\frac{\operatorname{Re}\xi_2 Gr_\theta \theta_0}{\xi_1} + \frac{\operatorname{Re}\xi_3 Gr_\phi \phi_0}{\xi_1} - 2\right)x + 1 \tag{53}$$

$$\theta_1 = -\frac{1}{2}\frac{\operatorname{Pr}\xi_6 R\theta_0}{\xi_5}x^2 - \left(\frac{1}{2}\frac{\operatorname{Pr}\xi_6 R\theta_0}{\xi_5} + 1\right)x + 1 \tag{54}$$

$$\phi_1 = -\frac{1}{2}\frac{ScK_0\phi_0}{\xi_6}x^2 + \left(\frac{1}{2}\frac{ScK_0\phi_0}{\xi_6}_{\,0} + 1\right)x + 1 \tag{55}$$

Solving equations (43) – (45) by applying the suitable boundary conditions from equation (49), the result implies.

$$u_2 = -\frac{1}{2}\frac{\operatorname{Re}\xi_2 Gr_\theta \theta_1}{\xi_1}x^2 - \frac{1}{2}\frac{\operatorname{Re}\xi_3 Gr_\phi \phi_1}{\xi_1}x^2 + \frac{1}{2}\left(\frac{\operatorname{Re}\xi_2 Gr_\theta \theta_1}{\xi_1} + \frac{\operatorname{Re}\xi_3 Gr_\phi \phi_1}{\xi_1} - 2\right)x + 1 \tag{56}$$

$$\theta_2 = -\frac{1}{2}\frac{\operatorname{Pr}\xi_6 R\theta_1}{\xi_5}x^2 - \left(\frac{1}{2}\frac{\operatorname{Pr}\xi_6 R\theta_1}{\xi_5} + 1\right)x + 1 \tag{57}$$

$$\phi_2 = -\frac{1}{2}\frac{ScK_0\phi_1}{\xi_6}x^2 + \left(\frac{1}{2}\frac{ScK_0\phi_1}{\xi_6} + 1\right)x + 1 \tag{58}$$

Solving equation (46) – (48) and imposing the appropriate boundary conditions from equation (49), the results yield.

$$u_3 = -\frac{1}{2}\frac{\operatorname{Re}\xi_2 Gr_\theta \theta_2}{\xi_1}x^2 - \frac{1}{2}\frac{\operatorname{Re}\xi_3 Gr_\phi \phi_2}{\xi_1}x^2 + \frac{1}{2}\left(\frac{\operatorname{Re}\xi_2 Gr_\theta \theta_2}{\xi_1} + \frac{\operatorname{Re}\xi_3 Gr_\phi \phi_2}{\xi_1} - 2\right)x + 1 \tag{59}$$

$$\theta_3 = -\frac{1}{2}\frac{\operatorname{Pr}\xi_6 R\theta_2}{\xi_5}x^2 - \left(\frac{1}{2}\frac{\operatorname{Pr}\xi_6 R\theta_2}{\xi_5} + 1\right)x + 1 \tag{60}$$

$$\phi_3 = -\frac{1}{2}\frac{ScK_0\phi_2}{\xi_6}x^2 + \left(\frac{1}{2}\frac{ScK_0\phi_2}{\xi_6} + 1\right)x + 1 \tag{61}$$

Equations (50) – (61) give the expressions for the velocity, temperature and concentration as

$$u = u_0 + u_1 + u_2 + u_3 + ...$$
$$\theta = \theta_0 + \theta_1 + \theta_2 + \theta_3 + ...$$
$$\phi = \phi_0 + \phi_1 + \phi_2 + \phi_3 + ... \quad (62)$$

Recasting equation (62), the results are

$$u = \frac{1}{8\xi_1\xi_5^2\xi_6^2}(-1+x)\left[\begin{array}{l}\left(\begin{array}{l}-4\left(8\xi_1 + \mathrm{Re}\,x(\lambda+\sigma)\xi_4\right)\xi_5^2 + \\ (-1+x)\,xGr_\theta\,\mathrm{Re}\,\xi_2\left(\begin{array}{l}R^2x^2(1+x)^2\,\mathrm{Pr}\,\xi_6^2 \\ -4Rx(1+x)\,\mathrm{Pr}\,\xi_6\xi_5 + 12\xi_5^2\end{array}\right)\end{array}\right)\xi_6^2 \\ +(-1+x)\,xGr_\phi\,\mathrm{Re}\,\xi_3\xi_5^2\left(x\left(2+3x+x^2\right)ScK_0^2 - 2x(3+2x)ScK_0\xi_6 + 12\xi_6^2\right)\end{array}\right] \quad (63)$$

$$\theta = \frac{1}{8\xi_5^3}(-1+x)\left[\begin{array}{l}\left(R^3x^3(1+x)^3\,\mathrm{Pr}\,\xi_6^3 - 4R^2x^2(1+2)^2\right)\mathrm{Pr}\,\xi_6^2\xi_5 \\ +12Rx(1+x)\,\mathrm{Pr}\,\xi_6\xi_5^2 - 32\xi_5^3\end{array}\right] \quad (64)$$

$$\phi = \frac{1}{8\xi_6^3}(-1+x)\left[\left(\begin{array}{l}x^3(1+x)(2+x)^2\,ScK_0^3 - 2x^2\left(6+7x+2x^2\right)ScK_0^2\xi_6 \\ +4x(5+3x)\,ScK_0\xi_6^2 - 32\xi_6^3\end{array}\right)\right] \quad (65)$$

RESULTS AND DISCUSSIONS

For better understanding of a physical problem and to explain the behaviour of various parameters used equations (63) – (65) with modified boundary conditions equations (20) are solved numerically utilising the values of dimensionless hydrodynamics parameters of scheme of different cases showcased in Table 1 and Table 2, The results of computations are showcased through the graph in Figures 2 - 16.

Concentration field

Figure 2 presents the concentration profiles ϕ along the boundary layer x for varying Schmidt numbers ($Sc = 1.5, 2.5, 3.5, 4.5, 5.5$) in the EMHD potassium dichromate nanofluid flowing through cylindrical coordinates. The results show that the increasing Schmidt number leads to a thinner concentration boundary layer, while lower values produce thicker profiles extending further into the flow.

At low (Sc) mass diffusion dominates over momentum transport, resulting in gradual changes in concentration across the boundary layer. Conversely, high (Sc) suppresses mass diffusion relative to momentum transport, confining the solute near the wall and producing steep concentration gradients. These trends are consistent with classical mass transfer theory and demonstrate the significant influence of the Schmidt number on species distribution in EMHD nanofluid flows. The analysis provides insight into the coupled heat and mass transfer behaviour of potassium dichromate nanofluids in cylindrical geometries under EMHD effects, offering a foundation for further theoretical and experimental investigations. The result agrees excellently with Gupta *et al*. (2025).

Figure 3 showcases the result of the concentration profile for varying values of the chemical reaction term, which shows that concentration decreases as displacement along the x-axis increases. The results also reveal that a decrease in concentration is caused by the increase in the chemical reaction term. The concentration of potassium dichromate ($K_2Cr_2O_7$) water base nanofluid increases as a result on increase in the dominance. Physically, the observed behaviour highlights the interplay between chemical reaction kinetics and mass diffusion in EMHD nanofluid flows. The reaction term directly influences the concentration distribution, which in turn affects local mass transfer rates and can modify coupled heat transfer characteristics in cylindrical geometries.

Figure 4 indicates the result of the concentration profile for varying values of nanoparticle volume fraction, showing

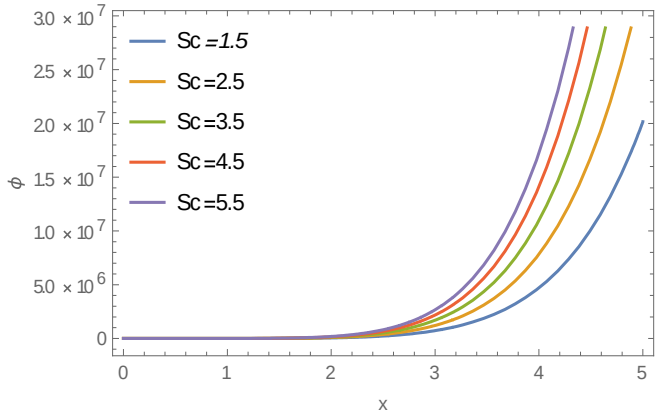

Figure 2. Concentration profile ϕ against boundary layer x for varying Schmidt number Sc.

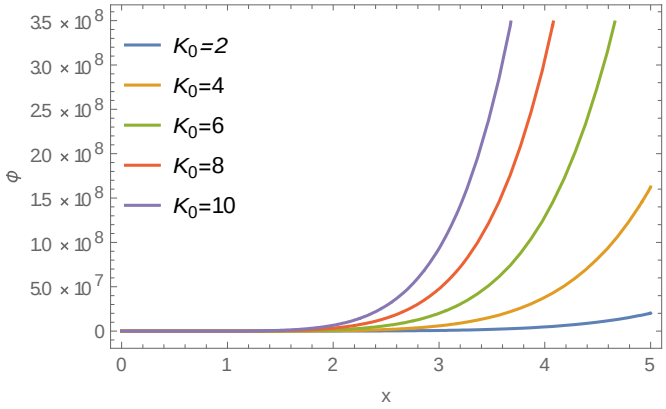

Figure 3. Concentration profile ϕ against boundary layer x for varying Chemical reaction term K_0.

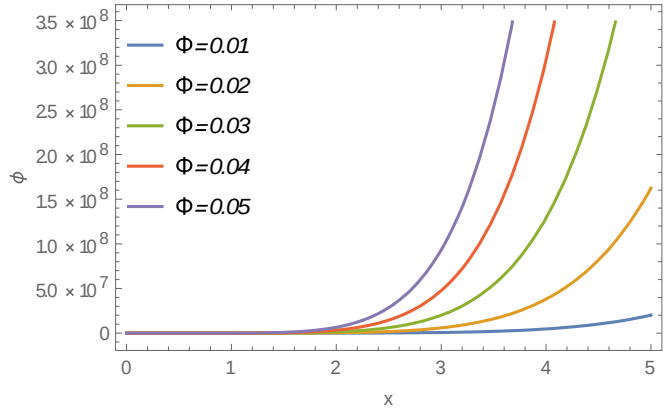

Figure 4. Concentration profile ϕ against boundary layer x for varying value of volume fraction.

that concentration decreases as displacement along the x-axis increases. Also observed from the result profile is the increase in concentration as the potassium dichromate

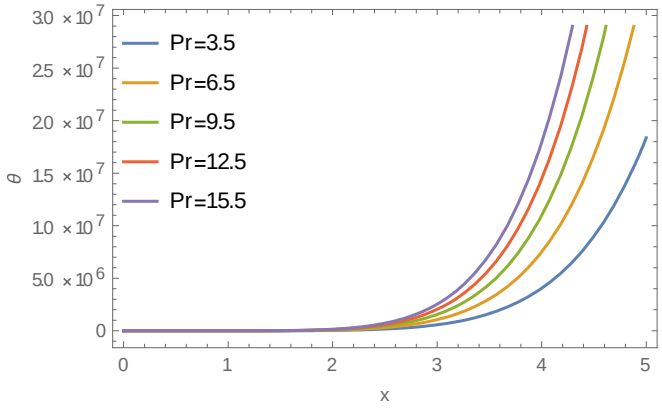

Figure 5. Temperature profile θ against boundary layer x for varying Prandtl number Pr.

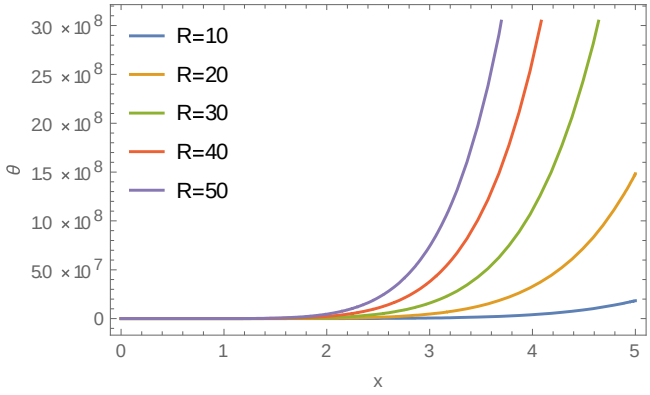

Figure 6. Temperature profile θ against boundary layer x for varying Radiation parameter R.

($K_2Cr_2O_7$) nanoparticle volume fraction increases. The observed behaviour arises from the coupling between nanofluid microstructure and mass transfer. Higher volume fractions increase the effective surface area and collision frequency between nanoparticles and solute molecules, enhancing convective-diffusive transport near the wall. In cylindrical EMHD flows, this effect interacts with Lorentz forces and the velocity field, modifying local species distribution and boundary layer development.

Temperature field

Figure 5 display pattern of trends that shows how temperature decreases as displacement along the *x*-axis increases. It was observed that when the Prandtl values are enhanced, the temperature profile drops. The results obtained imply that in a flow situation where momentum transfer dominates the thermal transfer motivated in the combined model, the temperature of potassium dichromate ($K_2Cr_2O_7$) water-based nanofluid increases as a result on increase in the dominance. This analysis

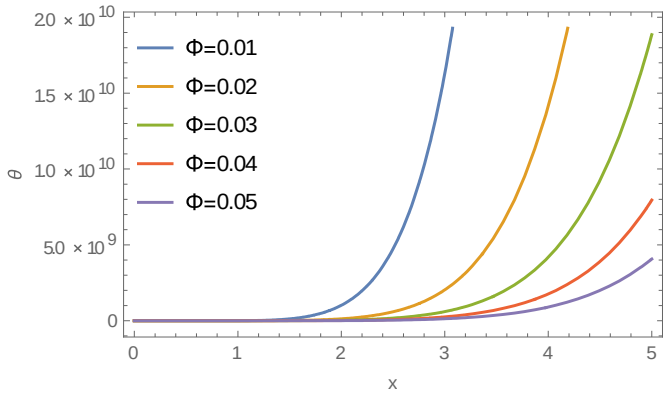

Figure 7. Temperature profile θ against boundary layer x for varying value of volume fraction.

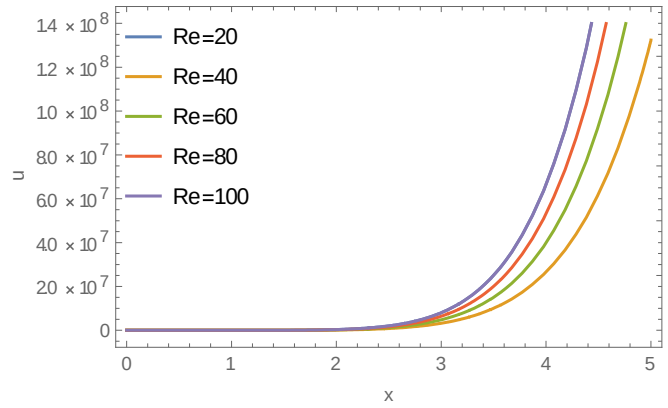

Figure 8. Velocity profile u against boundary layer x for varying Reynolds number Re.

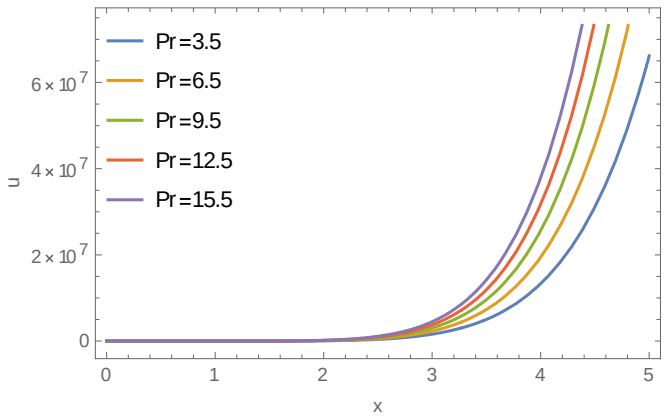

Figure 9. Velocity profile u against boundary layer x for varying Prandtl number Pr.

confirms that the Prandtl number is a key parameter controlling thermal transport in EMHD nanofluid flows, directly affecting the thermal boundary layer development and overall heat transfer performance.

Figure 6 profile of result obtained shows that temperature decreases as displacement along the x-axis increases, and drops further as the radiation term increases. Physically, the results obtained imply that the temperature of potassium dichromate ($K_2Cr_2O_7$) water-based nanofluid diminishes as a result on increase in the thermal layer. This result demonstrates that the thermal radiation parameter significantly influences the thermal boundary layer development and overall heat transfer performance in EMHD potassium dichromate nanofluid flows.

Figure 7 shows the results of the temperature profile of the nanofluid as the value of the nanoparticles volume fraction increases. The pattern of results obtained shows that as the nanoparticles' volume fraction increases, the temperature of our nanofluid samples is enhanced but diminishes along the axis. The physical implication of our result here is that in a situation where the concentration of potassium dichromate ($K_2Cr_2O_7$) nanoparticles increases in the base fluid, the temperature decreases along the axis, and increases slightly as the concentration of potassium dichromate ($K_2Cr_2O_7$) nanoparticles increases. The result presented for the combined thermal conductivity model is at a higher temperature value, as the volume fraction of potassium dichromate nanoparticle increases.

Velocity field

Figure 8 presents the graphical profile of velocity along the axis for increasing values of the Reynolds number. The behaviour of the results in the profile reveals how the velocity of the water base potassium dichromate ($K_2Cr_2O_7$) decreases for successive increases in values of Reynolds number. The pattern of results presented also shows that the velocity of potassium dichromate ($K_2Cr_2O_7$) nanofluid decreases along the axis for all values of the Reynold profile.

Figure 9 presents the graphical profile of velocity along the axis for increasing values of the Prandtl number. The pattern of results in the profile reveals how the velocity of the water-based potassium dichromate ($K_2Cr_2O_7$) also overlaps for a continuous increase in values of the Prandtl number. The pattern of results presented also shows that the velocity of Iron III oxide nanofluid decreases along the axis for all values of the Prandtl number.

Figure 10 presents the physical situation when the velocity profile is plotted along the axis for increasing Schmidt number values. The profile's result trend shows how the water-based potassium dichromate's velocity drops as Schmidt number values rise progressively. The pattern of results further demonstrates that, for all Schmidt number values, the velocity of the potassium dichromate ($K_2Cr_2O_7$) nanofluid drops along the axis.

Figure 11 presents the profile of velocity along the axis for increasing values of the Hartmann number. The pattern of results in the profile shows how the velocity of the water

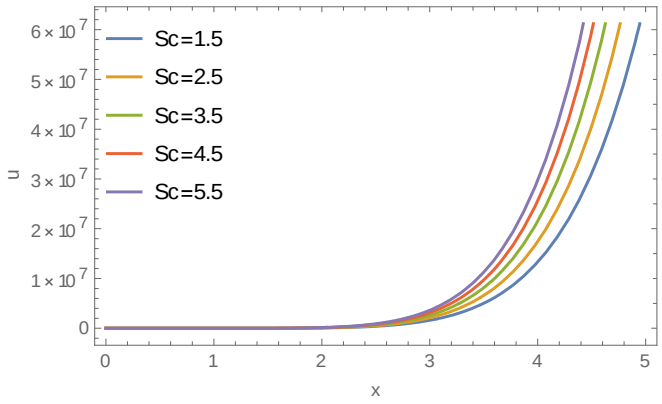

Figure 10. Velocity profile u against boundary layer x for varying Schmidt number Sc.

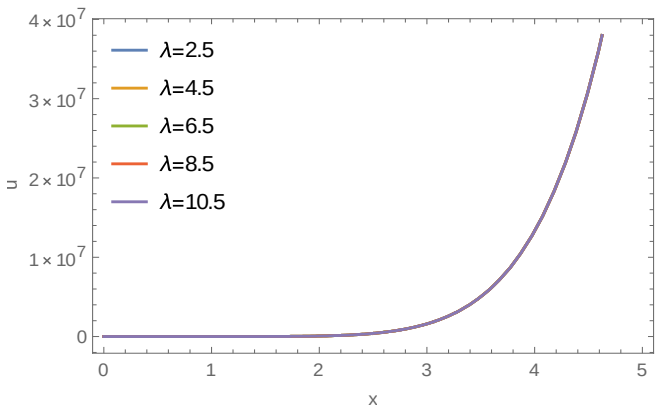

Figure 11. Velocity profile u against boundary layer x for varying Magnetic Hartmann number λ.

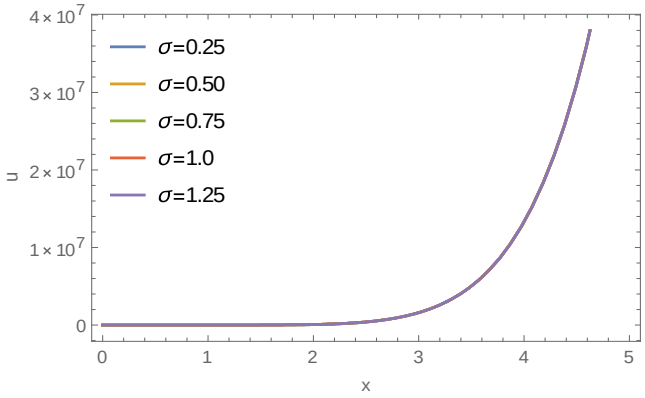

Figure 12. Velocity profile u against boundary layer x for varying Electroconductivity parameter σ.

base potassium dichromate increases for successive increases in values of the Hartmann number. The pattern of results presented also shows that the velocity of

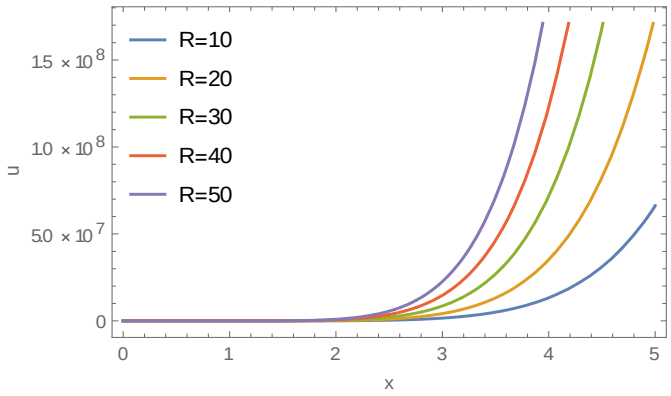

Figure 13. Velocity profile u against boundary layer x for varying Radiation parameter R.

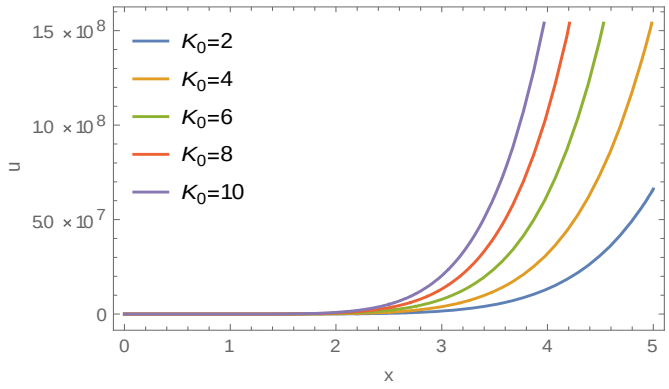

Figure 14. Velocity profile u against boundary layer x for varying Chemical reaction term K_0.

potassium dichromate ($K_2Cr_2O_7$) nanofluid decreases along the axis for all values of the Hartmann number.

Figure 12 presents the results of the velocity field for varying electroconductivity term show trendlines patterns that demonstrate how the velocity field decreases along the axis and diminishes further as the values of the electroconductivity term increase.

Figure 13 presents the trendlines showing how the water-based potassium dichromate's velocity is unresponsive to the subsequent rise in radiation parameter values. For all values of the radiation parameter, the pattern of results also demonstrates that the velocity of the potassium dichromate ($K_2Cr_2O_7$) nanofluid decreases down the axis.

Figure 14 presents the pattern of results in the profile of velocity along the axis for increasing values of the chemical reaction term. The pattern of results presented also shows that the velocity of potassium dichromate ($K_2Cr_2O_7$) nanofluid decreases along the axis for all values of the chemical reaction term. In terms of application, the influence of chemical reaction on velocity profiles is important for Microreactor flow control: Predicting how

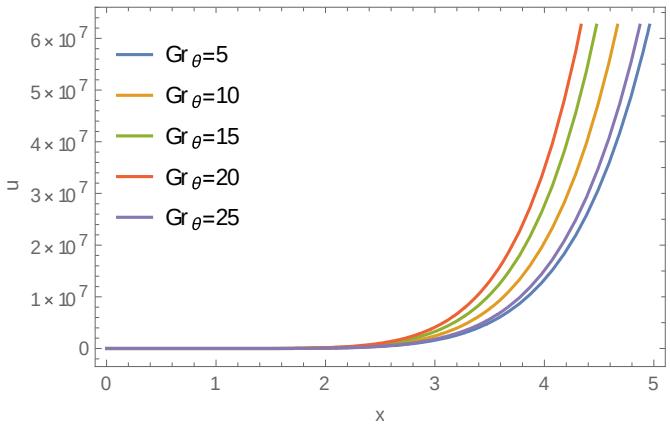

Figure 15. Velocity profile u against boundary layer x for varying Grashof number in term of temperature Gr_θ.

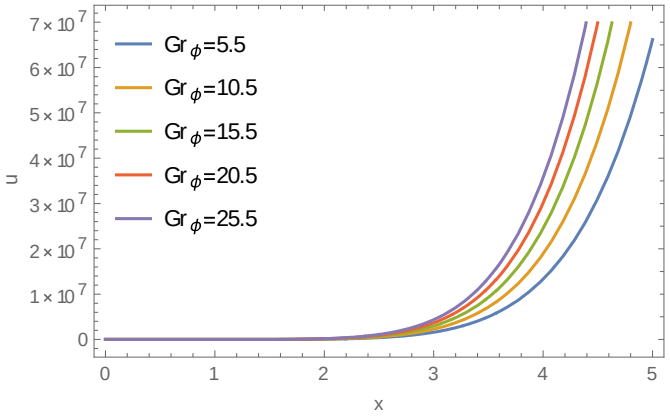

Figure 16. Velocity profile u against boundary layer x for varying Grashof number in term of concentration Gr_ϕ.

reactions affect momentum helps manage residence times and mixing. EMHD nanofluid systems: Coupled effects of chemical reaction and electromagnetic forces influence velocity, heat, and mass transport. Chemical processing and nanofluid cooling: Managing reaction rates can optimise flow profiles and improve the performance of cylindrical channels. These results demonstrate that chemical reaction rates, while primarily affecting species transport, indirectly influence momentum transport and boundary layer development in EMHD nanofluid flows.

Figure 15 showcased the impact of the velocity profile against the Grashof number due to temperature increase, which results about a significant increase in the velocity profile of the nanofluid. It was observed that the parameter for the modified Grashof due to temperature when it upraises, brings about a decrease in the velocity profile of the nanofluid. The result agrees excellently with Ojo and Egbo (2025).

Figure 16 indicates the effect of the Grashof parameter due to concentration on the velocity profile of the nanofluid. It was observed that when the Grashof number due to concentration differences improved upon, there is an increase in velocity profile, which affirmed the Grashof number as the fluid acted upon by a buoyancy force due to the dissimilarities in temperature. The outcome agrees excellently with the result of Ojo *et al.* (2025).

Conclusions

According to the mathematical assumption and formalism for nanofluid flow in a cylindrical coordinate using a combined model of effective thermal conductivity and effective viscosity, the behaviour of various material parameters such as the electroconductivity term, Radiation, Grashof's number, Schmidt number, Reynolds number and the Prandtl number, based on this present analysis, the following observations are made.

1. Velocity, temperature, and concentration boundary layers are strongly affected by fluid and transport parameters. Higher Reynolds and Grashof numbers enhance flow and convective transport, reducing boundary layer thickness.
2. Increase in nanoparticle volume fraction triggers an increase in concentration. Also, the water-based ($K_2Cr_2O_7$) velocity increases as the volume of nanoparticles increases.
3. Increasing Prandtl (Pr) and Schmidt (Sc) numbers produces thinner thermal and concentration boundary layers, while lower values allow stronger diffusion into the bulk.
4. Electromagnetic effects (Hartmann number H_a, electrical conductivity σ) suppresses velocity near the wall, thickening the boundary layer, whereas thermal radiation enhances temperature and slightly increases near-wall velocity.
5. Higher chemical reaction rates (K_o) reduce solute concentration near the wall, and increase nanoparticle volume fraction (φ) improves thermal conductivity, leading to steeper temperature gradients.
6. These findings provide insight into controlling flow, heat, and mass transfer in EMHD nanofluids, with applications in microfluidic reactors, nanofluid cooling, EMHD devices, and cylindrical heat exchangers.

CONFLICT OF INTEREST

The authors declare that they have no conflict of interest.

REFERENCES

Adetoye, S, O., Peter, O, N., Chijioke, A, E., & Edikan, S, U. (2026). The application of homotopy perturbation method in Newtonian fluids. *Fluid Mechanics*, 11(1), 1-11.

Adetoye, S., O., Alalibo, N., Micheal, O., & Chijioke Alloysius, E.

(2025). Energy transfer on magnetohydrodynamic silver nanofluid flow past a cylindrical enclosure. *Journal of Nanofluids*, *14*(5), 639-648.

Albqmi, N. M., & Sivanandam, S. (2024). Entropy generation and thermal radiation impact on magneto-convective flow of heat-generating hybrid nano-liquid in a non-Darcy porous medium with non-uniform heat flux. *Computation*, *12*(3), 43.

Ali, B., Naqvi, R. A., Haider, A., Hussain, D., & Hussain, S. (2020). Finite element study of mhd impacts on the rotating flow of casson nanofluid with the double diffusion Cattaneo—Christov heat flux model. *Mathematics*, *8*(9), 1555.

Aljaloud, A. S., Mumtaz, M. A., Rehman, S., & Ajmal, F. (2025). Machine learning data drive simulation for dual diffusive flow of stratified Maxwell fluid using Cattaneo-Christov heat flux and Darcy-Forchheimer model. *Results in Chemistry, 9,* 103016.

Batchelor, G. K. (1977). The effect of Brownian motion on the bulk stress in a suspension of spherical particles. *Journal of fluid mechanics*, *83*(1), 97-117.

Brinkman, H. C. (1949). A calculation of the viscous force exerted by a flowing fluid on a dense swarm of particles. *Flow, Turbulence and Combustion*, *1*(1), 27-34.

Cogley, A. C., Vincent, W. G., & Gilles, S. E. (1968). Differential approximation for radiative transfer in a nongrey gas near equilibrium. *Aiaa Journal*, *6*(3), 551-553.

Gupta, R., Albidah, A. B., Noor, N. F. M., & Khan, I. (2025). Application of DTM to heat source/sink in squeezing flow of iron oxide polymer nanofluid between electromagnetic surfaces. *Case Studies in Thermal Engineering*, *66*, 105735.

Hayat, T., Ullah, H., Ahmad, B., & Alhodaly, M. S. (2021). Heat transfer analysis in convective flow of Jeffrey nanofluid by vertical stretchable cylinder. *International Communications in Heat and Mass Transfer*, *120*, 104965.

He, J. H. (1999). Homotopy perturbation technique. *Computer methods in applied mechanics and engineering, 178*, 257-262.

Jameel, M., Shah, Z., Khan, M. S., & Ullah, N. (2024). Cattaneo-Christov heat flux model effect on magnetized Maxwell nanofluid flow over a stretching surface. *Materials Proceedings*, *17*(1), 12.

Jang, S. P., & Choi, S. U. S. (2007). Effects of various parameters on nanofluid thermal conductivity. Journal of Heat Transfer, *129*(5), 617-623.

Nikodijević Đorđević, M. D., Petrović, J. D., Kocić, M. M., Stamenković, Ž. M., & Nikodijević, D. D. (2025). EMHD flow and heat transfer of a nanofluid layer and a hybrid nanofluid layer in a horizontal channel with porous medium. *Applied Sciences*, *15*(18), 10183.

Ojo, A. S., & Egbo, C. A. (2025). Effect of radiation and chemical reaction on ozone layer healings. *Open Journal of Physical Science, 6*(2), 1-13.

Ojo, A. S., Alalibo, N. T., & Onyeaju, M.C. (2025). Numerical analysis of energy transfer on magnetohydrodynamic silver nanofluid flow in cylindrical coordinate. *Open Journal of Physical Science, 6*(1), 63-82.

Pheko, M., Goqo, S. P., Ahmedai, S., & Moleleki, L. (2025). Impact of Cattaneo–Christov Fluxes on Bio-Convective Flow of a Second-Grade Hybrid Nanofluid in a Porous Medium. *AppliedMath*, *5*(4), 180.

Tiwari, R. K., & Das, M. K. (2007). Heat transfer augmentation in a two-sided lid-driven differentially heated square cavity utilizing nanofluids. *International Journal of Heat and Mass Transfer*, *50*(9-10), 2002-2018.

Xue, Q. Z. (2005). Model for thermal conductivity of carbon nanotube-based composites. *Physica B: Condensed Matter*, *368*(1-4), 302-307.

Yasir, M., Khan, M. N., Saidani, T., & Alzahrani, A. (2025). Consequences of thermal radiation and entropy generation in magnetohydrodynamic Darcy-Forchheimer flow of nanomaterials. *Journal of Radiation Research and Applied Sciences, 18*(1), 101308.

Zahor, F. A., Jain, R., Ali, A. O., & Masanja, V. G. (2024). Entropy generation analysis of unsteady MHD nanofluid flow in a porous pipe. *International Journal of Thermofluids*, *24*, 100907.

Znaidia, S., Almuzaini, M., Rehman, S., Al-Malki, M. A., & Hashim. (2025). Sensitivity analysis of radiative heat transfer optimization in magnified radiative nanofluid flow past a melting surface: Effective viscosity and thermal conductivity. *Journal of Nonlinear Mathematical Physics*, *32*(1), 81.